



# Effect of substrates and post-deposition annealing on rf-sputtered Al-doped ZnO (AZO) thin films

Nalin Prashant Poddar<sup>1</sup> · S. K. Mukherjee<sup>1</sup>

Received: 10 April 2019 / Accepted: 2 July 2019 / Published online: 11 July 2019  
© Springer Science+Business Media, LLC, part of Springer Nature 2019

## Abstract

Al-doped zinc oxide (AZO) thin films were deposited on glass, quartz, and indium tin oxide (ITO) substrates using rf magnetron sputtering. The influence of the substrate material and post-deposition annealing (300–700 °C) in air on the structural, optical and electrical properties were studied. All as-deposited and annealed films were investigated using X-ray diffraction (XRD), grazing incidence XRD, field effect scanning electron microscope, Raman spectroscopy, UV–visible spectroscopy, Fourier transform infrared spectroscopy (FTIR), and four-point probe measurements. The AZO films were crystalline and preferentially oriented along the (002) diffraction plane. The average crystallite size decreased with annealing temperature and ranged from 19.6 to 30.3 nm. The AZO films were non-porous, dense, and continuous with columnar growth. The prominent Raman peaks showed anomalous doped ZnO modes. The deconvoluted Raman spectra showed the presence of  $A_1$  (LO) and  $A_1$  (TO) ZnO modes. FTIR revealed the Al–O and Zn–O stretching vibrations in the films. AZO films had high optical transmittance (61 to 78%) at visible wavelengths and an average band gap of  $3.27 \pm 0.04$  eV, which is suitable for optoelectronics applications. The resistivity ( $4.5 \times 10^{-4}$  to  $9 \times 10^{-4}$   $\Omega$  cm) and high figure of merit value indicates that AZO thin films may be suitable transparent conductive oxides.

## 1 Introduction

Transparent conductive oxide (TCO) films have been widely used in a variety of applications such as transparent electrodes for flat panel displays, solar cells, organic light emitting diodes (OLEDs), gas sensors and detectors. The most commonly used TCOs is indium tin oxide (ITO) [1]. However, indium is a rare and expensive material. Zinc oxide (ZnO) is one of the accepted TCOs, and has a wide band gap of 3.3 eV and low resistivity of  $2 \times 10^{-4}$   $\Omega$  cm which is similar to that of ITO films [2]. But in comparison with ITO, ZnO thin films have less stable electrical properties. Stable resistivity even at high temperature has been obtained by Al-doped ZnO (AZO) thin films. AZO thin films have been researched as a TCO due to its low cost, non-toxicity, and high thermal and chemical stability [3, 4].

AZO films have been deposited using many deposition techniques, such as magnetron sputtering [5], chemical vapour deposition (CVD) [6], metal organic CVD [7],

pulsed laser deposition [8], atomic layer deposition [9], electron beam evaporation [10], spray pyrolysis [11], vacuum arc deposition [12]. Apart from these, chemical routes like sol–gel [13], co-precipitation [14], hydrothermal [15], and chemical solution deposition techniques [16] are also used for synthesis AZO nanoparticles. Above all magnetron sputtering can produce uniform, highly oriented and textured AZO films at high deposition rate. Such preferentially oriented films have great influence on the TCOs properties [17]. These textured films can increase light scattering and hence, are highly beneficial for thin film solar cell applications [18].

AZO microstructure and their properties can be modified by controlling the deposition parameters, such as substrate temperature, deposition time (film thickness), sputtering power, gas flow rate and sputtering pressure [19–25]. Properties of grown AZO thin film depend on the types of substrates, surface topography, target to substrate distance, and the angle between the sputtering target and substrate holder [26, 27]. Most of the studies include the result of AZO films deposited on glass substrates [19–23, 25], while some also used Si, stainless steel,  $Al_2O_3$ , quartz and flexible substrates (polyimide film and polycarbonate) [19, 21, 24, 28–33]. Post-deposition annealing also affects the microstructural, optical and electrical properties of AZO films [31,

✉ Nalin Prashant Poddar  
nalinpoddar@gmail.com

<sup>1</sup> Department of Physics, Birla Institute of Technology, Mesra, Ranchi, Jharkhand 835215, India

32, 34–36]. All of these studies heat treated doped ZnO films in an Ar, N<sub>2</sub> or H<sub>2</sub> atmosphere. Some researchers reported the rapid thermal annealing of deposited films in O<sub>2</sub> and N<sub>2</sub> gases [37–39]. However, air annealing of sputtered AZO films has not been extensively studied [34, 36, 40]. Annealing of sputtered films in the air for a long time (more than 1 h) is scarcely documented. The effect of air annealing on the structural, optical and electrical properties of sputtered AZO films needs to be explored.

We have discussed the effect of AZO film thickness on the structural, optical, and electrical properties in our previous work [5]. The objective of the present work was to find the influence of the substrate material and post-deposition air annealing on the properties of rf sputtered AZO films. To verify the effect the structural, optical and electrical properties of all as-deposited and annealed films were investigated.

## 2 Experimental details

AZO thin films were deposited using a Plasma Consult MSC-3 rf magnetron sputtering system. The depositions were done using 3-inch diameter AZO target (Al 2 wt%) having purity 99.99%. Soda lime glass (2.5 × 2.5 × 0.2 cm), quartz (2.5 × 2.5 × 0.2 cm) and ITO (2.5 × 2.5 × 0.4 cm) substrates were placed just 80 mm above the target in a fixed substrate holder. All substrates were ultrasonically cleaned using isopropyl alcohol for 15 min and dried in air. Before deposition, the sputtering chamber evacuated down-to a base pressure  $2.5 \times 10^{-3}$  Pa using turbo molecular and rotary pumps. A pre-sputter cleaning of the AZO target was done for 5 min at 300 W in a 50 sccm Ar gas flow before each deposition. AZO films were deposited at a working pressure of 1.1 Pa, for 60 min using the Ar gas flow of 20 sccm. During the deposition, the sputter power was maintained at 200 W and the frequency was 13.56 MHz. All films were deposited at room temperature without any external substrate heating or substrate biasing. Complete deposition parameters are listed in Table 1. Post-deposition annealing of films was performed in an air furnace at 300–700 °C. The heating and cooling rate of the air furnace was 5 °C min<sup>-1</sup>. AZO films deposited on glass and ITO substrates were annealed at 500 °C for 6 h. AZO films deposited on quartz substrates were annealed for 6 h at 300, 500 and 700 °C, respectively. This temperature range was chosen since it is known as the maximum temperature range in device processing.

The crystallographic structure and phase orientations of all films were analyzed using conventional ( $\theta$ - $2\theta$ ) X-ray diffraction (XRD) and grazing incidence XRD (GIXRD) using a Rigaku SmartLab (9 kW) X-ray diffractometer with Cu K $\alpha$  radiation (0.154 nm). In conventional XRD, the scanning was done from 20° to 80° with  $2\theta$  steps of 0.04° in continuous mode. The GIXRD was carried out from 20°

**Table 1** AZO thin films deposition parameters

Process parameters	Values
Base pressure	$2.5 \times 10^{-3}$ Pa
Deposition pressure	1.1 Pa
Ar gas flow rate	20 sccm
rf power	200 W
Deposition time	60 min
Substrate	Quartz, glass, ITO
Distance between substrate holder and sputtering target	80 mm

to 80° at X-ray incidence angle  $\omega = 0.5^\circ$  and scanning step of 0.02°. The surface morphology and cross-section of the films were analyzed using a high-resolution ZEISS Sigma 300 field emission scanning electron microscope (FESEM). The film thickness was determined using the cross-sectional FESEM micrographs. Optical modes present in the deposited film were studied by Raman measurement in backscattering geometry at room temperature (298 K) using a Renishaw Invia-Raman Spectrometer. An Argon ion laser source with excitation wavelength 514.7 nm was used to analyze the samples. The spectra were collected for a wavenumber shifts of 200–800 cm<sup>-1</sup> with a data point acquisition time of 20 s. The transmittance spectra of the films were determined within the wavelength range 200–1000 nm using a UV-visible spectrometer (Perkin-Elmer, Lambda-25). The measurement was taken in transmittance mode at a scan speed of 240 nm min<sup>-1</sup>. The optical band gap of the AZO films was determined using Tauc's extrapolation method. The bonding present in the films was determined in the mid-infrared range of 400–4000 cm<sup>-1</sup> using Perkin-Elmer Frontier MIR spectrometer. The sheet resistance measurements of the films were done using linear four-point probe method with a probe spacing of 1 mm. A Keithley 2400 SourceMeter was used to source direct current into the films through the two outer probes and to sense the voltage developed in the films across the two inner probes. The resistivity was calculated from the sheet resistance and film thickness values.

## 3 Results and discussion

### 3.1 XRD studies

Figure 1a presents the XRD plots of as-deposited and annealed (500 °C in air) AZO films deposited on glass and ITO substrates. Figure 1b shows the XRD plots of AZO films deposited on a quartz substrate and annealed at different temperatures (300–700 °C in air). All films show a strong (002) diffraction peak at  $2\theta \sim 34.4^\circ$ . This peak corresponds to the wurtzite hexagonal phase of ZnO [4] and its complies

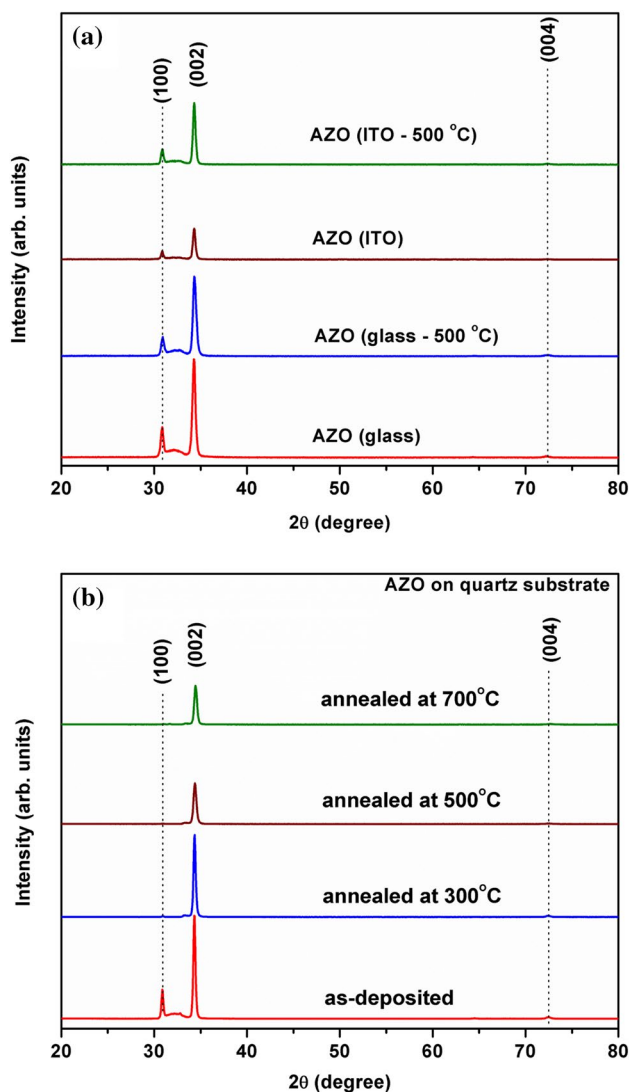


**Fig. 1** XRD plots of as-deposited and annealed AZO thin films deposited on—**a** glass and ITO substrates, and **b** quartz substrates

with JCPDS No. 36-1451. XRD peak with less intensity appeared at 30.9° (100) for as-deposited and annealed films

grown on glass and ITO substrates. This can also be seen on films deposited on quartz substrates, which disappeared after annealing. One more XRD peak with much less intensity appear at 72.4° (004) in all as-deposited and annealed AZO films. From the above observations, one can conclude that preferential growth in AZO films is not affected by the substrate materials.

Similar preferential growth in rf sputtered films were reported by several authors [20, 21, 28, 41, 42]. Preferential orientation in a film is influenced by the process of minimization of surface energy [5]. This growth in films could be explained by the “survival of fastest” model [43]. This model states that different crystal faces of a crystallite have different growth rates. The plane with minimum surface energy has the fastest growth rate [44, 45]. ZnO has minimum surface free energy along the (001) plane [42]. Thus, the preferred growth is detected parallel to the direction of (002) plane (*c*-axis).

Preferential growth in films is normally affected by deposition temperature [46] and working pressure [47]. The sputtering target has no effect on the crystalline structure of the thin films [5, 48]. The preferential growth is also not affected by the type of substrates [49, 50]. A. Wójcik et al. [49] observed ZnO with preferred orientation on crystalline *c*-Al<sub>2</sub>O<sub>3</sub>, amorphous lime glass and Si. Lee [50] developed preferentially oriented ZnO films on glass and polyimide substrates. Many others reported similar growth on a glass substrate [19–21, 23, 29, 41].

Figure 1b presents XRD plots of AZO films at different annealing temperatures. The intensity of the (002) peak decreased with increasing annealing temperature. On the other hand, the full width half maximum (FWHM) of the (002) diffraction peak increased from 0.274° (as-deposited) to 0.341° (annealed at 700 °C) with the annealing temperature. The FWHM of as-deposited AZO films was less than respective annealed films (see Table 2). In general, the crystal structure of AZO films is improved by post-deposition annealing [35, 37]. But in the present case, the XRD peak intensity of annealed films were lower

**Table 2** Crystallographic parameters of as-deposited and annealed AZO thin films

Substrate		2θ (°)	FWHM (°)	Crystallite size (nm)	d (Å)	Strain	Lattice parameters (Å)	
							a	c
Glass	As-deposited	34.28	0.348	21.6	2.614	0.003	3.012	5.229
	Annealed at 500 °C	34.32	0.423	19.6	2.611	0.002	3.015	5.223
ITO	As-deposited	34.32	0.328	25.3	2.611	0.002	3.016	5.223
	Annealed at 500 °C	34.32	0.337	24.6	2.611	0.002	3.016	5.223
Quartz	As-deposited	34.32	0.274	30.3	2.611	0.002	3.015	5.223
	Annealed at 300 °C	34.36	0.282	29.5	2.608	0.001	3.012	5.217
	Annealed at 500 °C	34.40	0.363	22.9	2.605	0	3.008	5.211
	Annealed at 700 °C	34.44	0.341	24.3	2.602	−0.001	3.005	5.205

than the as-deposited films. It means that the crystallinity can be achieved at room temperature in rf sputtered AZO films. The average crystallite size of the as-deposited and annealed films, corresponding to (002) phase was calculated using Scherrer's formula,

$$D_{av} = \frac{K\lambda}{\beta \cos \theta}, \quad (1)$$

where  $D_{av}$  is the average crystallite size,  $K$  is constant (0.9 for spherical grain),  $\lambda$  is the wavelength of X-ray,  $\beta$  is the FWHM of (002) diffraction peak. The average crystallite size along with FWHM of all as-deposited and annealed AZO films are listed in Table 2. The crystallite size of as-deposited AZO films decreases after post-deposition annealing. The average crystallite size decreases from 30.3 nm (as-deposited) to 24.3 nm (700 °C) with annealing temperature (see Table 2). Chen et al. [40] also reported a decrease in crystallite size after post-annealing in the air of ion beam sputtered AZO films. The decrease in crystallite size might be caused by the release of compressive stress or the oxidation of dopant Al (during annealing) present in the AZO film [40]. But, in XRD no  $\text{Al}_2\text{O}_3$  phase was detected; this indicates that either  $\text{Al}_2\text{O}_3$  is not present or if present, are XRD amorphous.

The (002) peak position of all as-deposited and annealed films were compared with that of the AZO target ( $2\theta = 34.4^\circ$ ) [5]. A peak shift of  $0.12^\circ$  to  $0.08^\circ$  toward lower  $2\theta$  value was observed for as-deposited and annealed AZO films deposited on glass, ITO and quartz substrates. The peak shifted towards higher  $2\theta$  value  $0.04^\circ$  for AZO film deposited on quartz and annealed at 700 °C. The ionic radius of  $\text{Al}^{3+}$  (53 pm) is smaller than  $\text{Zn}^{2+}$  (72 pm). During the deposition, smaller Al atoms may occupy Zn sites in the ZnO microstructure, producing a smaller cell size than in pure ZnO [24]. Hence the dopant concentration may be a reason for diffraction peak shift and broadening. In the present case, the dopant concentration was kept constant, as the films were deposited using AZO target (Al 2 wt%). Energy dispersive X-ray results also confirmed the presence of  $2.6 \pm 0.3\%$  Al in the deposited films [5]. Thus we can ignore the effect of peak shift due to doping. Apart from this, the films were always in uniform and non-uniform strain caused by grain structure and orientation depending upon the deposition parameters and process. The uniform strain generated in the film was determined using the following equation

$$\varepsilon = \frac{\Delta d}{d} = \frac{d_s - d_u}{d_u}, \quad (2)$$

where  $\varepsilon$  is the strain,  $d_u$  and  $d_s$  are the unstressed and stressed lattice spacing respectively. Here, for  $d_u$  the lattice spacing of the AZO sputtering target ( $2\theta = 34.4^\circ$ ) was used. The calculated strain is listed in Table 2.

The lattice parameters  $a$  and  $c$  of the hexagonal phase were evaluated using the relations concerned [51],

$$a = \frac{\lambda}{\sqrt{3} \sin \theta}, \quad (3)$$

$$c = \frac{\lambda}{\sin \theta}, \quad (4)$$

where  $\lambda$  is the X-ray wavelength and  $\theta$  is Bragg's angle. The calculated lattice parameters along with inter planer spacing ( $d$ ) are listed in Table 2. The obtained lattice parameters comply with JCPDS No. 36-1451 and other reported results [8, 15, 20, 35, 44, 49].

### 3.2 GIXRD studies

Figure 2a presents the GIXRD plots of as-deposited and annealed (500 °C in air) AZO films deposited on glass and ITO substrates. Figure 2b shows the GIXRD plots of AZO films deposited on a quartz substrate and annealed at different temperatures (300–700 °C in air). Using GIXRD one can probe thin films up to a specific depth that can add up information about all phases present in the material. GIXRD provides more details of the surface than the interior, so it is supposed that the surface or the top part of the thin films exhibited (103) texture. All as-deposited and annealed films show the (100) diffraction peak at  $31.1^\circ$ , (002) at  $34.4^\circ$ , (110) at  $56.2^\circ$ , and (103) diffraction peak at  $62.9^\circ$ . The (103) peak corresponds to the wurtzite hexagonal phase of ZnO [4] and also present in bulk AZO (sputtering target) [5]. The peak at  $62.9^\circ$  (103) was not visible in XRD spectra (see Fig. 1), but in GIXRD plots this peak evolved significantly (see Fig. 2). On the glass substrates, the (100) and (002) peaks were more prominent after annealing. While on the ITO substrates, the intensity of these two peaks was smaller after annealing. On the quartz substrates, the intensity of (103) GIXRD peak first increases upon annealing at 300 °C and then decreases after annealing at 500 °C and 700 °C. However, their FWHM remains constant at  $0.647^\circ \pm 0.029^\circ$ . The GIXRD peaks shifted  $0.16^\circ \pm 0.04^\circ$  towards higher  $2\theta$  values than the respective XRD peak positions.

The rf magnetron sputtering is a non-equilibrium process. During the sputtering, the atom deposited initially on the substrate will be covered by atoms deposited afterward. Hence, the atoms deposited at the end of the process are less restricted than the atoms deposited earlier, in that, the top surface atoms are free to move along the surface, the atoms deposited earlier do not reside on a free surface. The movement of these atoms over the film surface may destroy the crystallite orientation of the film. Thus, the growth of other planes could be possible. This may be one of the



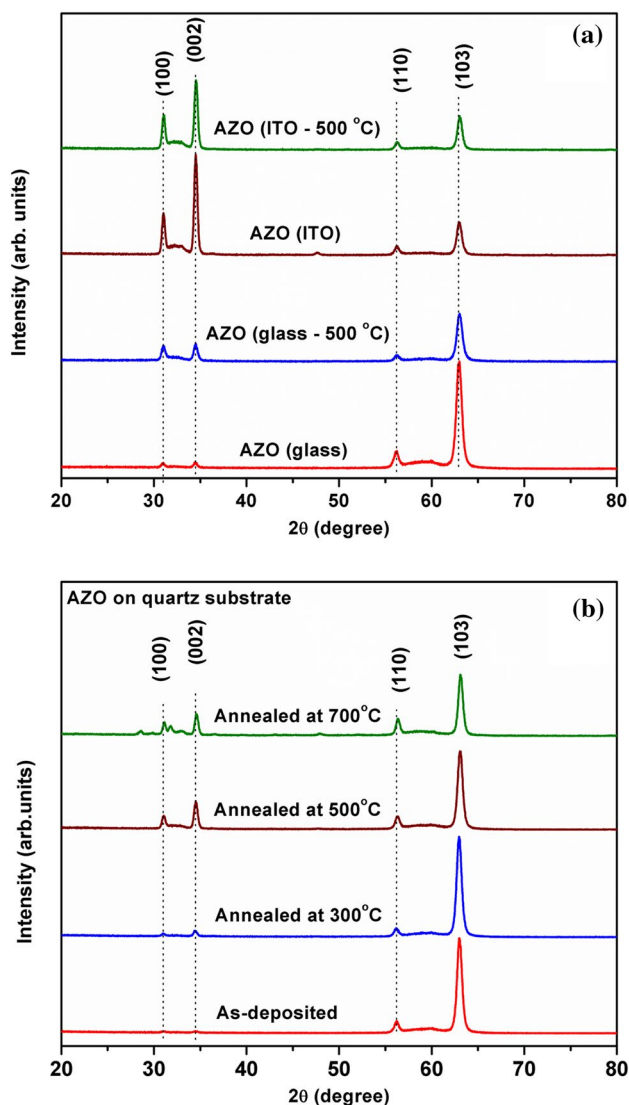


**Fig. 2** GIXRD plots of as-deposited and annealed AZO thin films deposited on—**a** glass and ITO substrates, and **b** quartz substrates

reasons behind the appearance of the (103) diffraction peak in GIXRD [52].

Wang et al. [52] reported conventional XRD and GIXRD peaks for rf sputtered ZnO films, and observed (103) peak in GIXRD, which is absent in XRD. They suggested that the origin of the (103) peak is related to the surface structure. They also observed that the (002) peak shifted towards a higher  $2\theta$  value in GIXRD in comparison with the XRD peak positions. With an increase in film thickness at higher deposition time, the number of the surface layer can possibly increase. Hence, using GIXRD more information about the surface layer instead of the bottom layer can be collected. As mentioned before, the (103) peak is related to the surface layer, increment in surface layers could be the reason behind the increase in the intensity of (103) peak with film

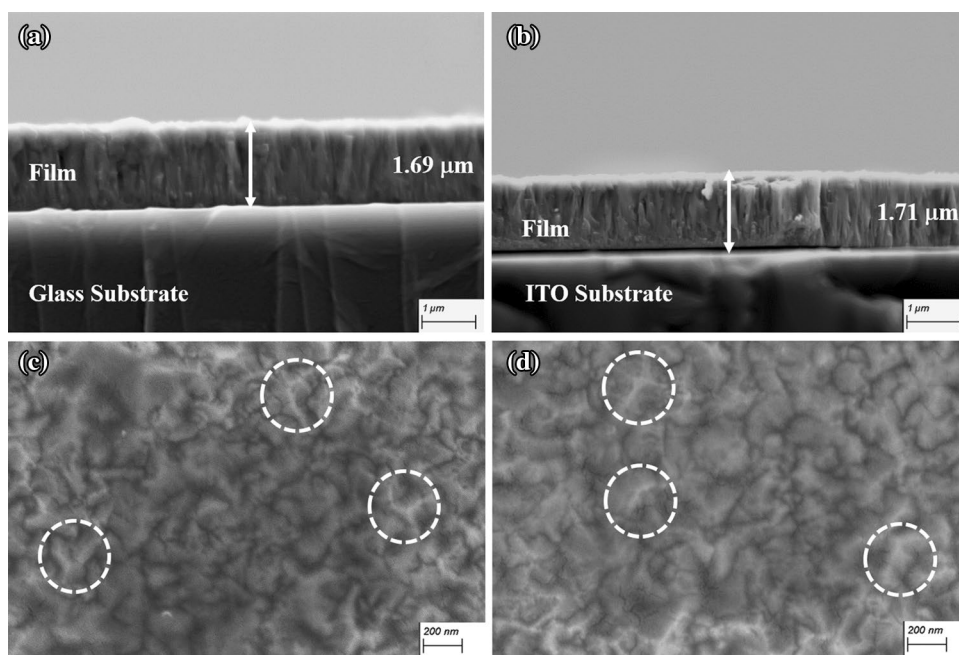
thickness. Li et al. [53] reported the columnar grain growth of rf sputtered ZnO films perpendicular to the glass substrate with cone-like crests. They suggested that the (103) texture might be related to the cone-like crests of crystal grains. Chang et al. [54] reported the presence of (103) GIXRD peak for In-doped ZnO thin films deposited using atmospheric pressure plasma jet on a glass substrate. D. H. Lee et al. reported the (103) diffraction peak for rf sputtered Ga-doped ZnO films [55]. Thus, we can conclude that the (103) diffraction peak appears in both un-doped [52, 53] and doped ZnO [54, 55]. Yue et al. [56] reported that the intensity of the (002) peak increased with increasing deposition pressure and the (103) peak first increased and then decreased as the deposition pressure was increased ( $\leq 1.0$  Pa). Meljanac et al. [57] reported (002), (103) peaks along with other diffraction peaks for AZO films deposited using sputtering and annealed at temperature in the range of 200–400 °C.

### 3.3 FESEM studies

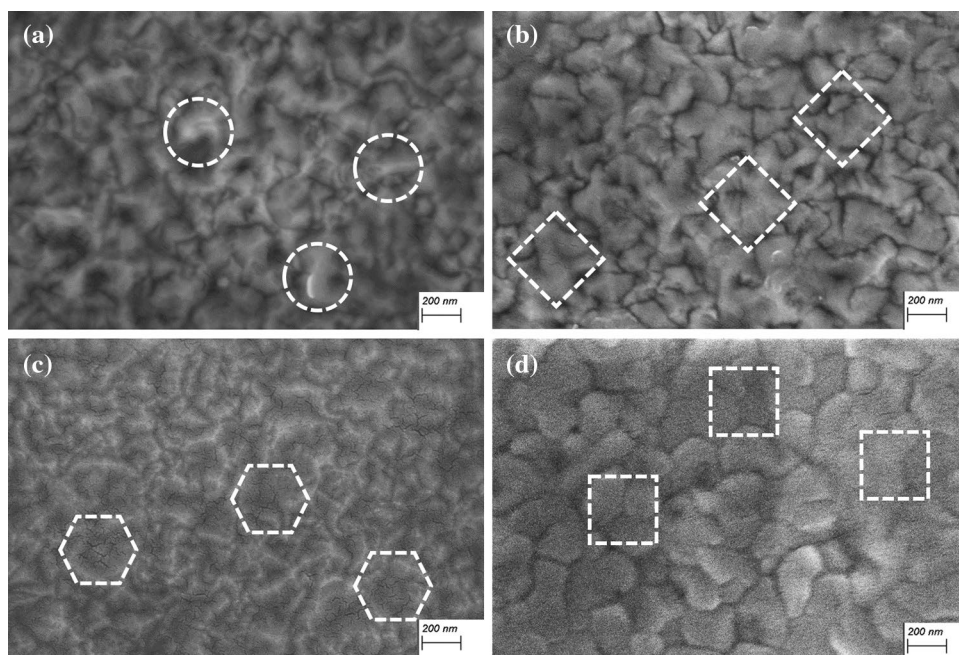
Figure 3 represents cross-sectional and surface FESEM micrographs of the as-deposited AZO films deposited on glass and ITO substrates. The thickness of all of the films was the same,  $1.7 \pm 0.01$   $\mu\text{m}$  (see Fig. 3a, b). The average deposition rate was deduced from film thickness and deposition time to be  $28.3 \pm 0.1$   $\text{nm min}^{-1}$ . The cross-section shows perpendicular unidirectional growth of the film over the substrate. A similar structure was observed for rf sputtered AZO films deposited on glass substrates in our previous work [5]. This columnar growth appears more arranged over the crystalline ITO substrate than on amorphous glass substrate. The columns are well-connected indicating dense films. B. C. Mohanty et al. reported similar flake-like structure for rf sputtered AZO films deposited at 50–200 W [44].

Figure 3c, d show the surface morphology of as-deposited AZO film deposited on glass and ITO substrates, respectively. Figure 4 shows FESEM micrographs of as-deposited AZO films deposited on a quartz substrate and annealed at different temperatures. The as-deposited films on glass, ITO and quartz substrates (Figs. 3c, d, and 4a, respectively) had equal thickness and their surface appears similar. Different surface morphologies were observed with increasing annealing temperature. All the as-deposited films were uniform, continuous and dense. No porosity was observed. The film surface appeared rough with sharp hills and valleys like patterns (marked with a circle in Figs. 3c, d, and 4a, respectively). The grain boundaries were very distinct and could be observed as dark black lines. The hill like pattern was less sharp after annealing (marked with a rhombus in Fig. 4b). A similar surface morphology was reported by Zhang et al. [25] for AZO film deposited at substrate temperatures of 100 °C and 150 °C. With increasing annealing temperature, the grain

**Fig. 3** FESEM of AZO thin films—**a** cross-sectional micrograph of a film deposited on a glass substrate, **b** cross-sectional micrograph of a film deposited on an ITO substrate, **c** surface micrograph of a film deposited on a glass substrate, and **d** surface micrograph of a film deposited on an ITO substrate



**Fig. 4** FESEM micrograph of AZO thin films deposited on a quartz substrate—**a** as-deposited, **b** annealed at 300 °C, **c** annealed at 500 °C, and **d** annealed at 700 °C



boundaries disappears and fine cracks appeared across the film surface (marked with a hexagon in Fig. 4c). The film annealed at 700 °C showed collapsed grain boundaries (marked with a square in Fig. 4d). The hill-like patterns were replaced by large grains with no sharp tip and disconnected grain boundaries.

### 3.4 Raman spectroscopy studies

It should be noted that the profile and position of Raman peaks depend on the crystallization, residual stress and structural disorder of films. Group theory predicts the

presence of the following optical lattice phonons in wurtzite ZnO crystal structure [58]

$$1A_1 + 2B_1 + 1E_1 + 2E_2, \quad (5)$$

where the  $A_1$  and  $E_1$  modes are polar and can split into transverse optical (TO) and longitudinal optical (LO) phonons, both being active in Raman and infrared spectroscopy.  $B_1$  modes are infrared and Raman inactive (silent modes). The two nonpolar modes, low-frequency  $E_2$  (low), and high frequency  $E_2$  (high), are Raman active.

Figure 5 shows the Raman scattering spectra of as-deposited and annealed AZO films deposited on glass and ITO substrates. Three distinct Raman peaks at  $276 \pm 2 \text{ cm}^{-1}$ ,  $514 \pm 2 \text{ cm}^{-1}$  and  $582 \pm 4 \text{ cm}^{-1}$  were observed. All Raman spectra were deconvoluted using a sum of Lorentzian function (see Fig. 5). After deconvolution additional peaks could be realized at  $388 \pm 1$ ,  $455 \pm 3$ ,  $562 \pm 5$ ,  $645 \pm 1 \text{ cm}^{-1}$ . Figure 6 depict the Raman scattering spectra of AZO films deposited on a quartz substrate and annealed at different temperatures. Prominent Raman peak appears at  $276 \pm 2 \text{ cm}^{-1}$ ,  $513 \pm 2 \text{ cm}^{-1}$ , and  $582 \pm 1 \text{ cm}^{-1}$ . These peaks are the characteristics of doped ZnO [5]. Other Raman modes at  $375 \pm 5$ ,  $449 \pm 7$ ,  $562 \pm 1$  and  $646 \pm 1 \text{ cm}^{-1}$  were detected after deconvolution (see Fig. 6).

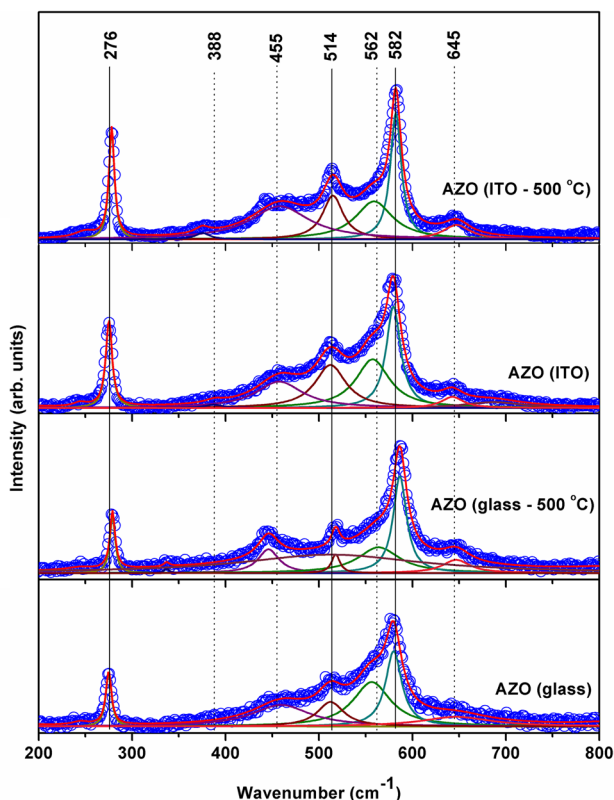


**Fig. 5** Raman spectra (together with fitting curves) of as-deposited and annealed (500 °C) AZO thin films deposited on glass and ITO substrates

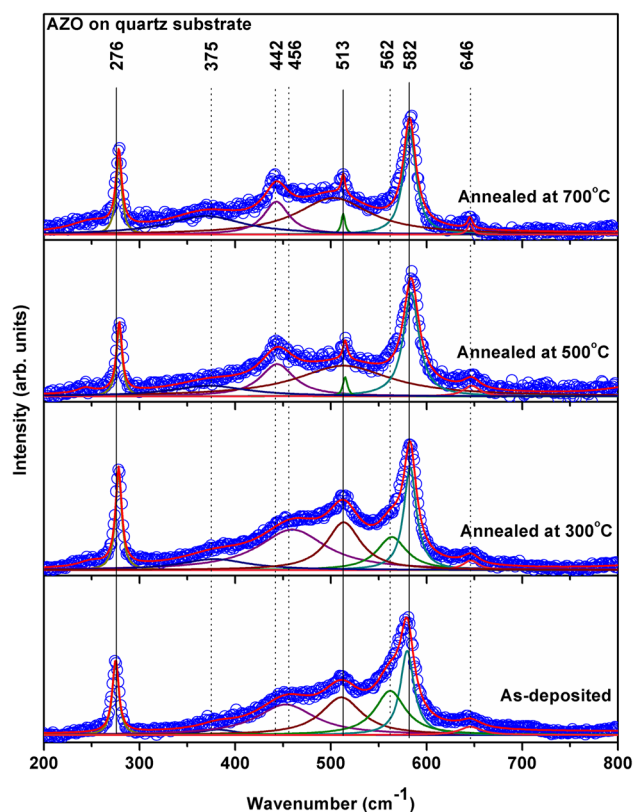


**Fig. 6** Raman spectra (together with fitting curves) of as-deposited and annealed (300–700 °C) AZO thin films deposited on a quartz substrate

The peak at  $388 \pm 1 \text{ cm}^{-1}$  and  $375 \pm 5 \text{ cm}^{-1}$  correspond to  $A_1$  (TO) mode of ZnO. The peak at  $562 \pm 5 \text{ cm}^{-1}$  and  $562 \pm 1 \text{ cm}^{-1}$  belongs to  $A_1$  (LO) mode of ZnO. All other observed peaks correspond to anomalous Raman modes which appears due to doping in ZnO. All observed Raman peaks are consistent with the reported peak positions [5, 44]. Raman peaks which correspond to anomalous modes are common in doped ZnO films and are absent in un-doped ZnO films. These modes cannot be correlated to any particular dopant material and are assumed to be disorder-activated modes [5]. Hence one can conclude that the anomalous modes present in as-deposited and annealed AZO films are associated with the Al dopant.

### 3.5 UV–visible spectroscopy studies

Figure 7a shows the optical transmittance of as-deposited and annealed AZO films deposited on glass and ITO substrates. Figure 7b present the optical transmittance of as-deposited and annealed (300–700 °C) AZO films deposited on a quartz substrate. All AZO films were transparent to visible light with an average transmittance 61–73% (at 550 nm). The transmittance has a fluctuating wave like spectrum due



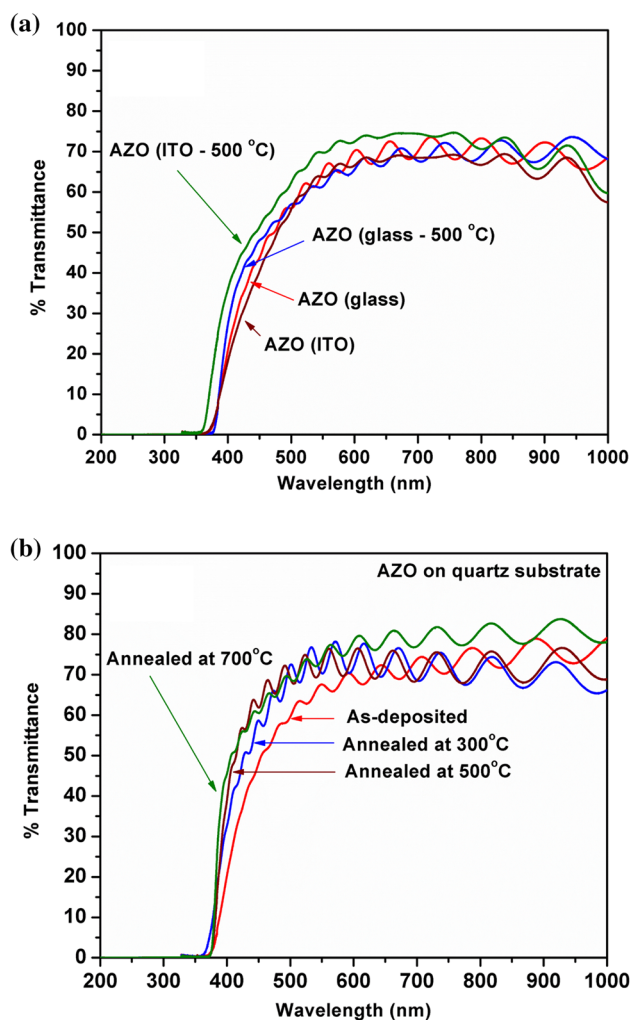


**Fig. 7** Optical transmittance of as-deposited and annealed AZO thin films deposited on—**a** glass and ITO substrates, and **b** quartz substrates

to the interference generated from the reflection at the film interfaces [23]. A slight increase in transmittance after annealing was observed. The optical transmittance for as-deposited and annealed AZO films deposited on glass, ITO and quartz substrates at 550 nm, 620 nm, and 700 nm are listed in Table 3.

The optical transmittance depends on film thickness, amounts of  $\text{Al}_2\text{O}_3$  and the film crystallinity [29]. In the present work, the deposition parameters and the target material were kept constant. Therefore, the little variation of optical transmittance for films on various substrates could be attributed to the variations in the crystallinity of the films. It has been observed that the crystalline structure of thin films improves with an increment of annealing temperature. Hence the optical transmittance should increase with post-deposition annealing [35, 38]. XRD analysis showed that the crystallinity of AZO films changed slightly with substrates and annealing temperatures (see Fig. 1a, b). This might be a reason for variation in optical transmittance of films deposited at different substrates. The film crystallinity decreased with annealing in air (see Fig. 1b). Therefore the decrease in transmittance is expected [40]. But, a slight increment in optical transmittance was observed after post-deposition annealing (see Fig. 7b). The transmittance of films annealed in an oxygen-rich environment is higher than the vacuum annealed films [53]. This variation occurs due to the different concentration of oxygen vacancies present in the post-annealed films. Annealing in an oxygen rich atmosphere may increase oxygen absorption in the film that improves optical transmittance.

Lee et al. [28] reported 85% transmittance for 200 nm AZO film deposited on PET substrate at different sputtering power. They observed that the average transmittance slightly decreased with an increase in sputtering power. Kim et al. [22] observed 80–85% transmittance for 250 nm thick films deposited at different sputtering pressures on

**Table 3** Optical and electrical properties of as-deposited and annealed AZO thin films

Substrate	% Transmittance			Band gap (eV)	Sheet resistance ( $\Omega/\text{sq}$ )	Resistivity ( $10^{-4} \Omega \text{ cm}$ )	Figure of merit ( $10^4 \Omega^{-1} \text{ cm}^{-1}$ )
	(At 550 nm)	(At 620 nm)	(At 700 nm)				
<b>Glass</b>							
As-deposited	65.09	67.50	70.04	3.23	5.9	9.0	$7.5 \pm 0.27$
Annealed at 500 °C	61.39	68.46	67.67	3.24	–	–	–
<b>ITO</b>							
As-deposited	63.76	68.52	68.46	3.26	2.9	4.5	$14.6 \pm 0.59$
Annealed at 500 °C	69.74	73.98	74.44	3.35	–	–	–
<b>Quartz</b>							
As-deposited	67.59	68.01	73.79	3.27	4.6	7.1	$9.8 \pm 0.48$
Annealed at 300 °C	70.32	77.23	68.58	3.31	4.5	6.9	$10.4 \pm 0.65$
Annealed at 500 °C	72.23	72.50	68.58	3.24	–	–	–
Annealed at 700 °C	73.90	78.04	77.03	3.26	–	–	–



glass substrates. Optical transmittance decreased with increasing working pressure [22, 41]. Optical transmittance decreased with increasing film thickness due to an increase in scattering, reflection and optical absorption [5, 23]. Yang et al. [32] deposited AZO on quartz substrates using sputtering and studied the post-annealing effect in  $N_2$  and  $N_2 + H_2$  environment. They reported an average transmittance of 85–95% for AZO film with a thickness of 250 nm. The transmittance decreased with increasing annealing temperature [32]. Yang et al. [24] deposited 250 nm AZO film on quartz at different rf powers, substrate to target distances and Ar flow rates and observed optical transmittances of 80–95%. Fu et al. [21] reported a decrease in optical transmittance with an increase of substrate temperature. Li et al. [33] deposited AZO on quartz and glass substrates, and observed a high transmittance of 90%. It became 80% for film deposited on a  $SiO_2$  buffer layer.

The band gap can be calculated with the help of absorption coefficient using this equation

$$\alpha h\nu = \alpha_0 (h\nu - E_g)^n, \quad (6)$$

where  $\alpha$  is the absorption coefficient,  $h\nu$  is photon energy,  $\alpha_0$  is a constant whose value does not depend on  $h\nu$  and  $n$ ,  $E_g$  is the optical band gap and  $n$  is an index characterizing the type of electronic transition:  $n = 2$  for the indirect allowed transitions, and  $n = 1/2$  for direct allowed transitions. AZO has a direct band gap. The value of direct optical band gap was obtained by plotting  $(\alpha h\nu)^2$  versus  $h\nu$  in the high absorbance region. Figure 8a, b show the Tauc plot of all as-deposited and annealed AZO films. By extrapolating the linear portion of the plot to the  $x$ -axis  $E_g$  was calculated, and is listed in Table 3.

The calculated band gap of as-deposited and annealed AZO films ranged from 3.23 to 3.35 eV. The band gap of AZO films deposited on glass and ITO substrates increased after annealing. Decrease in the film crystallinity after annealing could be the reason behind this [23]. But, the band gap of AZO thin film deposited on a quartz substrate decreased at higher annealing temperature (500–700 °C). This could be due to increase in resistivity (see Table 3) and decrease in carrier concentration at higher annealing temperature. A similar change in band gap is reported by Chen et al. [40] after post-deposition annealing of AZO films in air.

The obtained band gap value is similar to the band gap of bulk un-doped ZnO (3.3 eV) [59], but is smaller than those reported by L. Dejam et al. (3.4–4 eV) [35], N. E. Duygulu et al. (3.65 eV) [19], D. K. Kim et al. (3.52–3.94 eV) [22], W. Yang et al. (3.76–3.86 eV) [24], H. Tong et al. (3.46–3.74 eV) [36], M. Sucheai et al. (3.35–3.43 eV) [48], and J. H. Lee (3.51–3.64 eV) [50]. The obtained band gap value is similar and slightly larger than those reported by

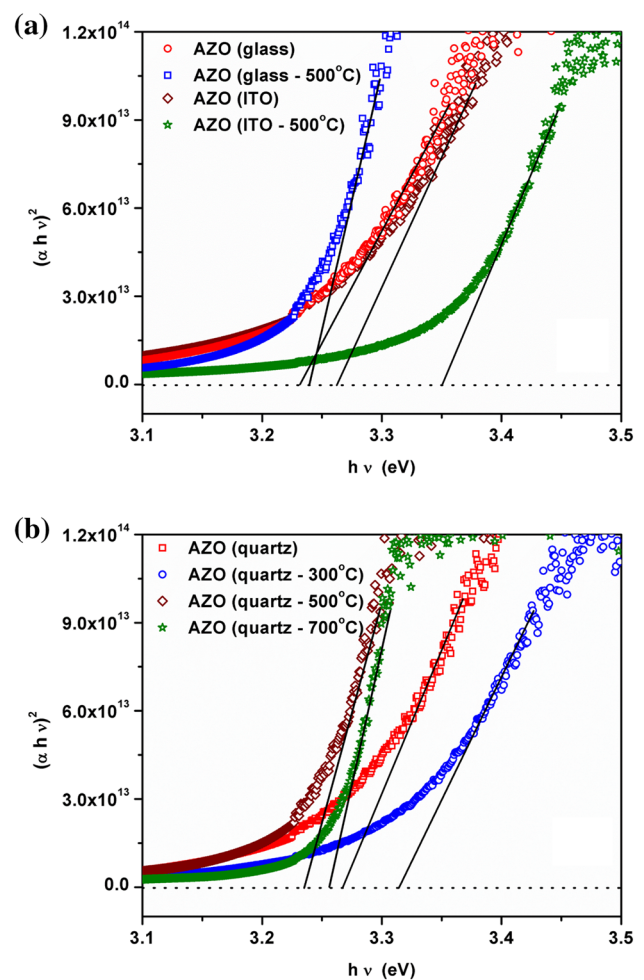


**Fig. 8** Tauc plot  $(\alpha h\nu)^2$  versus  $h\nu$  of as-deposited and annealed AZO thin films deposited on—**a** glass and ITO substrates, and **b** quartz substrates

X. Li et al. (3.27 eV) [53], D. Meljanac et al. (2.85–3.0 eV) [57], and S. H. Jeong et al. (3.18–3.36 eV) [26].

### 3.6 FTIR spectroscopy studies

Figure 9a, b shows the infrared spectra of as-deposited and annealed AZO films deposited on glass, ITO and quartz substrates. The Fourier transform infrared (FTIR) spectra had a series of transmission bands in the range of 400–4000  $cm^{-1}$ . Broad absorption can be seen at different wavenumbers. The absorption is due to the vibrational modes of bonds between Al, Zn and O present in the films. Strong absorption in the FTIR spectra was observed in the films between 400 and 600  $cm^{-1}$  [15]. This absorption can be correlated with Zn–O stretching vibrations. The stretching vibrational mode of Zn–O bonds have been reported at variable wavenumbers within 400–575  $cm^{-1}$  [11, 13, 15, 60–63]. This confirms the presence of Zn–O bond of as-deposited and annealed AZO

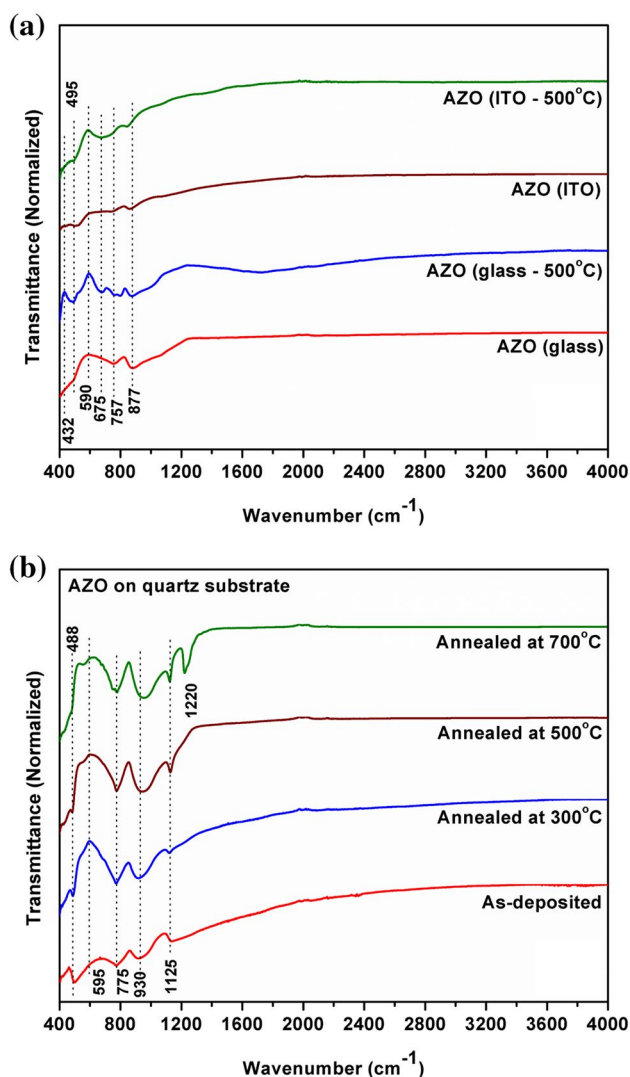


**Fig. 9** FTIR spectra (in MIR region) of as-deposited and annealed AZO thin films deposited on—**a** glass and ITO substrates, and **b** quartz substrates

films. Absorption bands appearing at  $590\text{ cm}^{-1}$ ,  $595\text{ cm}^{-1}$  and  $675\text{ cm}^{-1}$  are associated with Al–O bond [64, 65]. Peaks at about  $757\text{ cm}^{-1}$  and  $775\text{ cm}^{-1}$  is an Al–O indicator [5]. The peak at  $1125\text{ cm}^{-1}$  may correspond to Zn–O and Al–O stretching vibrations [64].

### 3.7 Electrical properties

The resistivity values of AZO films were determined using the film thickness and sheet resistance. Figure 10a shows the resistivity ( $\rho$ ) of as-deposited AZO films deposited on glass, ITO and quartz substrates. The sheet resistance of each film was obtained by plotting current (I) versus voltage (V) using a four-point probe set-up. The individual values of sheet resistance and resistivity are listed in Table 3. The resistivity

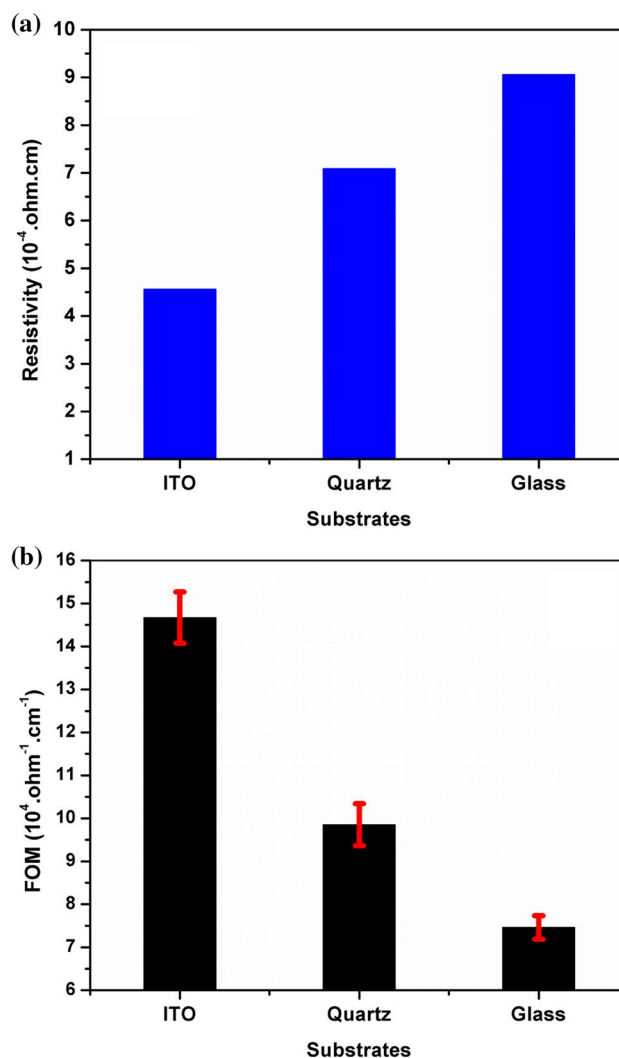


**Fig. 10** **a** Resistivity of as-deposited AZO thin films deposited on glass, ITO and quartz substrates and **b** FOM of as-deposited AZO thin films deposited on glass, ITO and quartz substrates

of films annealed at a higher temperature ( $> 300\text{ }^{\circ}\text{C}$ ) are more than the as-deposited films and could not be obtained using the four-point probe set-up. The calculated resistivity ranged from  $4.5 \times 10^{-4}$  to  $9 \times 10^{-4}\ \Omega\ \text{cm}$ . The resistivity of the film deposited on the ITO substrate ( $4.5 \times 10^{-4}\ \Omega\ \text{cm}$ ) was the lowest. The ITO substrate is conductive and has a resistivity in the order of  $10^{-4}\ \Omega\ \text{cm}$  [1].

The resistivity of AZO films depends upon effective doping of Al into the ZnO lattice. Replacement of  $\text{Zn}^{2+}$  ion by  $\text{Al}^{3+}$  generates one electron as charge carrier. The number of charge carriers can be enhanced by increasing the dopant concentration [9]. But, in the present case, the dopant (Al) concentration was fixed, as the films were deposited with the same sputtering target and deposition parameters. The thickness of the deposited films was also the same. Hence, the effect of dopant concentration and film thickness on resistivity is ruled out. From

XRD and FESEM it is observed that different substrates and post-deposition annealing had some influence on the crystallinity and surface morphology of the AZO films. These may be the reason behind the variation of resistivity with substrates [33]. The crystallinity of the annealed films was less than the as-deposited films. Cracks and disconnected grain boundaries appeared in the films annealed at high temperature. Annealing in air may also enhance the oxygen absorption in the film [40]. This could increase the resistivity of the film annealed at high temperatures.

The resistivity of sputtered AZO films increases with increasing rf power [20], base pressure [22], and working pressure [41]. The resistivity decreases with increasing substrate temperature during sputtering [21], film thickness [5, 23, 45] and annealing temperature [32]. Low resistivity values, of the order of  $10^{-4}$ – $10^{-3}$   $\Omega$  cm were reported by several authors [10, 12, 19–22, 24, 25, 27, 28, 32–34]. Hou et al. [9] reported resistivity of  $2.38 \times 10^{-3}$   $\Omega$  cm for the AZO film deposited with 2.26% Al content. They mentioned that the resistivity initially decreased with Al concentration, but at high Al concentration its resistivity increased due to degeneration of the crystal quality. Li et al. [33] reported the variation of resistivity of 100 nm AZO films deposited on different substrates using sputtering. They observed the resistivity of  $5.14 \times 10^{-4}$   $\Omega$  cm and  $9.1 \times 10^{-4}$   $\Omega$  cm for AZO film deposited on quartz and glass substrates, respectively. The resistivity also depends on the post-deposition annealing environment. Tong et al. [36] reported that rf sputtered AZO film annealed in the air had higher resistivity than films annealed in  $N_2$  and  $H_2$  environments. Chen et al. [40] reported an increase in resistivity of AZO film after annealing in air. This may happen due to the presence of more oxygen atoms on the AZO film surfaces, trapping electrons.

A figure of merit (FOM) was defined as the ratio of transmittance to the resistivity, and calculated using the following equation [19, 22]

$$FOM = \frac{\%T}{\rho}, \quad (7)$$

where %T is the average percentage transmittance in the visible spectrum (400–700 nm) and  $\rho$  ( $\Omega$  cm) is the resistivity of the AZO films. Figure 10b shows the FOM of as-deposited AZO films deposited on glass, ITO and quartz substrates. The FOM ranged from  $7.5 \times 10^4$  and  $14.6 \times 10^4$   $\Omega^{-1}$   $cm^{-1}$ . The calculated FOM value is similar to that of N. E. Duygulu et al. ( $3.0 \times 10^4$ – $7.8 \times 10^4$   $\Omega^{-1}$   $cm^{-1}$ ) [19] and D. K. Kim et al. ( $2.4 \times 10^4$ – $12 \times 10^4$   $\Omega^{-1}$   $cm^{-1}$ ) [22].

## 4 Conclusion

All deposited AZO films were preferentially oriented ( $2\theta = 34.4^\circ$ ) along the (002) plane irrespective of film deposition substrates. A peak shift of  $0.12^\circ$ – $0.08^\circ$  toward lower  $2\theta$  value was observed for as-deposited AZO films. The peak (002) shifted  $0.04^\circ$  towards higher  $2\theta$  value for the film deposited on quartz and annealed at  $700^\circ C$ . The average crystallite size decreased with annealing temperature and ranged from 19.6 to 30.3 nm. GIXRD showed the presence of the (103) diffraction peak at  $2\theta = 62.9^\circ$ , absent in XRD plots. The GIXRD peaks were at higher values of  $2\theta$  by  $0.16^\circ \pm 0.04^\circ$  than the XRD peak positions. FESEM micrographs indicated columnar AZO film growth on different substrates. The grain boundaries disappeared and collapsed at high annealing temperature. The deconvoluted Raman spectra of as-deposited and annealed films revealed  $A_1$  (LO) and  $A_1$  (TO) modes of wurtzite ZnO. Anomalous doped ZnO modes was indicated by distinct Raman peaks at  $276 \pm 2$ ,  $514 \pm 2$ , and  $582 \pm 4$   $cm^{-1}$ . FTIR results showed Al–O and Zn–O stretching vibrations in the AZO films. The optical transmittance of the AZO films ranged from 61 to 74% at 550 nm. The calculated electrical resistivity of as-deposited films was in the range of  $4.5 \times 10^{-4}$  to  $9 \times 10^{-4}$   $\Omega$  cm. The average optical band gap of as-deposited and annealed AZO films was  $3.27 \pm 0.04$  eV. The FOM ranged from  $7.5 \pm 0.27 \times 10^4$  to  $14.6 \pm 0.59 \times 10^4$   $\Omega^{-1}$   $cm^{-1}$ . These results support the possibility of using AZO films as transparent electrodes in OLEDs, solar cells and other optoelectronic devices.

**Acknowledgements** The authors acknowledge the Central Instrumental Facility (CIF) of Birla Institute of Technology, Ranchi for their support in characterizations work. One of the authors (Nalin Prashant Poddar) thanks the Birla Institute of Technology, Ranchi for the Award of an Institute Fellowship.

## References

1. T. Minami, T. Miyata, *Thin Solid Films* **517**, 1474–1477 (2008)
2. T. Minami, *MRS Bull.* **25**, 38–44 (2000)
3. T. Minami, H. Nanto, S. Takata, *Appl. Phys. Lett.* **41**, 958–960 (1982)
4. H. Nanto, T. Minami, S. Shooji, S. Takata, *J. Appl. Phys.* **55**, 1029–1034 (1984)
5. N.P. Poddar, S. Mukherjee, *J. Mater. Sci. Mater. Electron.* **30**, 537–548 (2019)
6. T.M.K. Thandavan, S.M.A. Gani, C. San Wong, R.M. Nor, *PLoS ONE* **10**, e0121756 (2015)
7. A. Nebatti, C. Pflictsch, B. Atakan, *Thin Solid Films* **636**, 532–536 (2017)
8. S. Venkatachalam, Y. Iida, Y. Kanno, *Superlattices Microstruct.* **44**, 127–135 (2008)
9. Q. Hou, F. Meng, J. Sun, *Nanoscale Res. Lett.* **8**, 144 (2013)

10. D. Sahu, S.Y. Lin, J.L. Huang, *Microelectron. J.* **38**, 245–250 (2007)
11. A. Djelloul, M.S. Aida, J. Bougdira, *J. Lumin.* **130**, 2113–2117 (2010)
12. T. Miyata, Y. Minamino, S. Ida, T. Minami, *J. Vac. Sci. Technol. A* **22**, 1711–1715 (2004)
13. S.S. Alias, A.B. Ismail, A.A. Mohamad, *J. Alloys Compd.* **499**, 231–237 (2010)
14. L. Cai, G. Jiang, C. Zhu, D. Wang, *Phys. Status Solidi A* **206**, 1461–1464 (2009)
15. N.R. Yogamalar, A.C. Bose, *J. Alloys Compd.* **509**, 8493–8500 (2011)
16. S.B. Majumder, M. Jain, P.S. Dabal, R.S. Katiyar, *Mater. Sci. Eng. B* **103**, 16–25 (2003)
17. D.S. Ginley, C. Bright, *MRS Bull.* **25**, 15–18 (2000)
18. S.E. Pust, J.P. Becker, J. Worbs, S.O. Klemm, K.J. Mayrhofer, J. Hüpkens, *J. Electrochem. Soc.* **158**, D413–D419 (2011)
19. N.E. Duygulu, A. Kodolbas, A. Ekerim, *J. Cryst. Growth* **394**, 116–125 (2014)
20. S.Y. Kuo, K.C. Liu, F.I. Lai, J.F. Yang, W.C. Chen, M.Y. Hsieh, H.I. Lin, W.T. Lin, *Microelectron. Reliab.* **50**, 730–733 (2010)
21. E.G. Fu, D.M. Zhuang, G. Zhang, W.F. Yang, M. Zhao, *Appl. Surf. Sci.* **217**, 88–94 (2003)
22. D.K. Kim, H.B. Kim, *J. Alloys Compd.* **522**, 69–73 (2012)
23. B.L. Zhu, S.J. Zhu, J. Wang, J. Wu, D.W. Zeng, C.S. Xie, *Physica E* **43**, 1738–1745 (2011)
24. W. Yang, Z. Liu, D.L. Peng, F. Zhang, H. Huang, Y. Xie, Z. Wu, *Appl. Surf. Sci.* **255**, 5669–5673 (2009)
25. Z. Zhang, C. Bao, W. Yao, S. Ma, L. Zhang, S. Hou, *Superlattices Microstruct.* **49**, 644–653 (2011)
26. S.H. Jeong, J.H. Boo, *Thin Solid Films* **447**, 105–110 (2004)
27. J.W. Leem, J.S. Yu, *Thin Solid Films* **518**, 6285–6288 (2010)
28. J. Lee, D. Lee, D. Lim, K. Yang, *Thin Solid Films* **515**, 6094–6098 (2007)
29. X. Wang, X. Zeng, D. Huang, X. Zhang, Q. Li, *J. Mater. Sci. Mater. Electron.* **23**, 1580–1586 (2012)
30. J.J. Ding, H.X. Chen, S.Y. Ma, *Physica E* **42**, 1861–1864 (2010)
31. C.H. Choi, S.H. Kim, *J. Cryst. Growth* **283**, 170–179 (2005)
32. W. Yang, Z. Wu, Z. Liu, A. Pang, Y.-L. Tu, Z.C. Feng, *Thin Solid Films* **519**, 31–36 (2010)
33. C. Li, M. Furuta, T. Matsuda, T. Hiramatsu, H. Furuta, T. Hirao, *Thin Solid Films* **517**, 3265–3268 (2009)
34. T.H. Chen, T.C. Cheng, Z.R. Hu, *Microsyst. Technol.* **19**, 1787–1790 (2013)
35. L. Dejam, S.M. Elahi, H.H. Nazari, H. Elahi, S. Solaymani, A. Ghaderi, *J. Mater. Sci. Mater. Electron.* **27**, 685–696 (2016)
36. H. Tong, Z. Deng, Z. Liu, C. Huang, J. Huang, H. Lan, C. Wang, Y. Cao, *Appl. Surf. Sci.* **257**, 4906–4911 (2011)
37. H.J. Cho, S.U. Lee, B. Hong, Y.D. Shin, J.Y. Ju, H.D. Kim, M. Park, W.S. Choi, *Thin Solid Films* **518**, 2941–2944 (2010)
38. J. Kim, J.H. Yun, S.W. Jee, Y.C. Park, M. Ju, S. Han, Y. Kim, J.H. Kim, W.A. Anderson, J.H. Lee, J. Yi, *Mater. Lett.* **65**, 786–789 (2011)
39. Y.C. Cheng, *Appl. Surf. Sci.* **258**, 604–607 (2011)
40. Y.Y. Chen, P.W. Wang, J.C. Hsu, C.Y. Lee, *Vacuum* **87**, 227–231 (2013)
41. S.N. Bai, T.Y. Tseng, *J. Mater. Sci. Mater. Electron.* **20**, 253–256 (2009)
42. S.S. Lin, J.L. Huang, *Surf. Coat. Technol.* **185**, 222–227 (2004)
43. A. Van der Drift, *Philips Res. Rep.* **22**, 267–269 (1967)
44. B.C. Mohanty, B.K. Kim, D.H. Yeon, Y.H. Jo, I.J. Choi, S.M. Lee, Y.S. Cho, *J. Electrochem. Soc.* **159**, H96–H101 (2011)
45. K.H. Ri, Y. Wang, W.L. Zhou, J.X. Gao, X.J. Wang, J. Yu, *Appl. Surf. Sci.* **258**, 1283–1289 (2011)
46. S.Y. Pung, K.L. Choy, X. Hou, C. Shan, *Nanotechnology* **19**, 435609 (2008)
47. C.C. Ting, S.Y. Chen, D.M. Liu, *Thin Solid Films* **402**, 290–295 (2002)
48. M. Suche, S. Christoulakis, N. Katsarakis, T. Kitsopoulos, G. Kiriakidis, *Thin Solid Films* **515**, 6562–6566 (2007)
49. A. Wójcik, M. Godlewski, E. Guziewicz, R. Minikayev, W. Paszkowicz, *J. Cryst. Growth* **310**, 284–289 (2008)
50. J.-H. Lee, *J. Electroceram.* **23**, 512 (2009)
51. A. Purohit, S. Chander, A. Sharma, S.P. Nehra, M.S. Dhaka, *Opt. Mater.* **49**, 51–58 (2015)
52. Y. Wang, X. Li, G. Jiang, W. Liu, C. Zhu, *J. Mater. Sci. Mater. Electron.* **24**, 3764–3767 (2013)
53. X. Li, Y. Wang, W. Liu, G. Jiang, C. Zhu, *Mater. Lett.* **85**, 25–28 (2012)
54. K.M. Chang, S.H. Huang, C.J. Wu, W.L. Lin, W.C. Chen, C.W. Chi, J.W. Lin, C.C. Chang, *Thin Solid Films* **519**, 5114–5117 (2011)
55. D.H. Lee, K. Kim, Y.S. Chun, S. Kim, S.Y. Lee, *Curr. Appl. Phys.* **12**, 586–590 (2012)
56. H. Yue, A. Wu, Y. Feng, X. Zhang, T. Li, *Thin Solid Films* **519**, 5577–5581 (2011)
57. D. Meljanac, K. Juraić, V. Mandić, H. Skenderović, S. Bernstorff, J.R. Plaisier, A. Šantić, A. Gajović, B. Šantić, D. Gracin, *Surf. Coat. Technol.* **321**, 292–299 (2017)
58. J. Calleja, M. Cardona, *Phys. Rev. B* **16**, 3753 (1977)
59. Ü. Özgür, Y.I. Alivov, C. Liu, A. Teke, M. Reshchikov, S. Doğan, V. Avrutin, S.-J. Cho, H. Morkoç, *J. Appl. Phys.* **98**, 11 (2005)
60. P.K. Kannan, R. Saraswathi, J.B.B. Rayappan, *Sens. Actuators A* **164**, 8–14 (2010)
61. A. Srivastava, Praveen, M. Arora, S.K. Gupta, B.R. Chakraborty, S. Chandra, S. Toyoda, H. Bahadur, *J. Mater. Sci. Technol.* **26**, 986–990 (2010)
62. F. Meriche, T. Touam, A. Chelouche, M. Dehimi, J. Solard, A. Fischer, A. Boudrioua, L.H. Peng, *Electron. Mater. Lett.* **11**, 862–870 (2015)
63. R. Menon, V. Gupta, H.H. Tan, K. Sreenivas, C. Jagadish, *J. Appl. Phys.* **109**, 064905 (2011)
64. Y. Li, J. Wang, Y. Kong, J. Zhou, J. Wu, G. Wang, H. Bi, X. Wu, W. Qin, Q. Li, *Sci. Rep.* **6**, 19187 (2016)
65. A. Mallika, A.R. Reddy, K.S. Babu, K.V. Reddy, *Ceram. Int.* **40**, 12171–12177 (2014)

**Publisher's Note** Springer Nature remains neutral with regard to jurisdictional claims in published maps and institutional affiliations.